PCCP

Intense deep-red zero phonon line emission of Mn4+ in double perovskite La4Ti3O12

Journal:	*Physical Chemistry Chemical Physics*
Manuscript ID	CP-ART-07-2019-004007.R2
Article Type:	Paper
Date Submitted by the Author:	24-Sep-2019
Complete List of Authors:	Ji, Haipeng; Zhengzhou University, School of Materials Science and Engineering; Kyoto University, Graduate School of Human and Environmental Studies Ueda, Jumpei; Kyoto University, Brik, Mikhail; Tartu Ulikool, Institute of Physics Du, Mao Hua ; Oak Ridge National Laboratory, Chen, Deliang; Zhengzhou University, School of Materials Science and Engineering Tanabe, Setsuhisa; kyoto university, Grad School of HES; Kyoto University

Intense deep-red zero phonon line emission of Mn^{4+} in double perovskite $La_4Ti_3O_{12}$

Haipeng Ji,[1,2,*,//] Jumpei Ueda,[2,//] Mikhail G. Brik,[3,4] Mao-Hua Du,[5] Deliang Chen,[1,**] Setsuhisa Tanabe[2]

[//] H. Ji and J. Ueda contributed equally.

[1] School of Materials Science and Engineering, Zhengzhou University, Zhengzhou 450001, China

[2] Graduate School of Human and Environmental Studies, Kyoto University, Kyoto 606-8501, Japan

[3] College of Sciences, Chongqing University of Posts and Telecommunications, Chongqing 400065, China

[4] Institute of Physics, University of Tartu, Tartu 50411, Estonia

[5] Materials Science & Technology Division, Oak Ridge, TN 37831, USA

Corresponding authors:

[*]Haipeng Ji (jihp@zzu.edu.cn [HJ]), and [**]Deliang Chen (dlchen@zzu.edu.cn [DC])

Abstract

Phosphors that emit in deep-red spectral region is critical for the plant cultivation lighting-emitting diodes. Herein, ultrabroadband deep-red luminescence of Mn^{4+} in $La_4Ti_3O_{12}$ was studied which showed intense zero phonon line emission. The double-perovskite structural $La_4Ti_3O_{12}$ simultaneously contains two Ti^{4+} sites forming slightly- and highly-distorted TiO_6 octahedrons, respectively. The influence of octahedron distortion on the Mn^{4+} emission energy in the two distinct Ti^{4+} sites was studied both experimentally and theoretically. The spectroscopy measurement indicated that Mn^{4+} in $La_4Ti_3O_{12}$ showed intense zero phonon line emission (ZPL) at deep-red 710-740 nm under excitation of 400 nm charging the $O^{2-} \rightarrow Mn^{4+}$ charge transfer transition. The splitting of the ZPL of the Mn^{4+} $^2E_g \rightarrow {}^4A_{2g}$ transition as well as the intensity of ZPL relative to the vibronic phonon sideband emissions were found to be greatly influenced by the octahedral distortion degree. The crystal-field strength and Racah parameters of Mn^{4+} in each Ti^{4+} sites were also estimated. The Mn^{4+} $^2E_g \rightarrow {}^4A_{2g}$ luminescence exhibited severe thermal quenching, which was explained by the low-lying $^4T_{2g}$ level and charge-transfer state.

Keywords Mn^{4+}, Luminescence, Double perovskite, Titanate

1 Introduction

The Mn^{4+} ion with $3d^3$ electronic configuration prefers to occupy octahedral sites due to the attainment of large crystal filed stabilization energy which allows the three 3*d* electrons occupying the three t_{2g} orbitals.[1] The Mn^{4+} *d-d* transition in the red (620-650 nm) or deep-red spectral region (710-740 nm) has been proposed for general lighting or plant cultivation lighting-emitting diodes, respectively.[2,3,4] The Mn^{4+} 3*d* electrons locate in an outer orbit and the luminescence of the *d-d* transition is thus sensitive to the bonding ligands and their geometrical arrangement.

Due to a high effective positive charge, Mn^{4+} tends to experience a large crystal field strength and no transition from the $^4T_{2g}$ level is expected. The electronic transition from the ^2E_g level to the ground $^4A_{2g}$ level is both parity- and spin-forbidden, which could become partially allowed *via* an "intensity borrowing" mechanism[5]: the ^2E_g state mixes with the $^4T_{2g}$ state by spin-orbit interaction and then the wave function of the ^2E_g contains a small contribution from the $^4T_{2g}$ state. The sharp-line emissions consist of vibrionic phonon sidebands and zero phonon line (ZPL). Moreover, it is suggested that the spin-selection rule can be further relaxed if the Mn^{4+} occupies a distorted octahedron site,[6] with Mn^{4+} shifting from the inversion center either approaching an octahedron vertex, an edge or a facet. Thus, the transition probability determining the ZPL intensity would be affected by the octahedron distortion. Besides, the strength of the anion-p/Mn^{4+}-3d covalent mixing is also affected by the distortion.[7] The energetical position of the emitting ^2E_g state is almost independent on the crystal filed strength but highly dependent on the covalency of the "Mn^{4+}-ligand" bonding. The $^2E_g \rightarrow {}^4A_{2g}$ transition energy changes little in the ionic fluoride hosts but varies greatly in oxides, since the covalence variation in fluorides is much smaller than that in oxides.[8] Moreover, the "Mn^{4+}-O^{2-}" covalent mixing has been claimed to be influenced by connectivity of the octahedral moieties and deviation of O-Mn-O bond angle from 90°.[9]

Typical structures such as spinel, inverse spinel, perovskite, double perovskite, rock salt, pyrochlore, bixbyite hold octahedral coordination[10] which can accommodate and stabilize Mn^{4+} ions. Among the aforesaid compounds, the double-perovskite structural $La_4Ti_3O_{12}$ is of particular interest, since it simultaneously accommodates slightly- and highly-distorted TiO_6 octahedrons. As far as we know, although the influence of octahedron distortion on the Mn^{4+} ZPL energy has been studied among a group of perovskite hosts with various compositions and lattice parameters,[7] the study of such effect within one single host compound containing two different octahedral sites has not been conducted yet. The purpose of this study is to explore the effect of octahedron distortion on the Mn^{4+} $^2E_g \rightarrow {}^4A_{2g}$ luminescence and the covalent interaction between Mn^{4+} and O^{2-} ions at both Ti^{4+} sites of $La_4Ti_3O_{12}$. Properties

such as the crystal-filed splitting (10*Dq*) and the electron-electron (Racah) parameters *B* and *C* were also comparatively estimated. The Mn^{4+} luminescence in $La_4Ti_3O_{12}$ exhibits severe thermal quenching which finds no practical application, but the spectroscopic study may be theoretically inspiring for developing new Mn^{4+}-doped phosphors.

2 Experimental and computation

Preparation. Non-doped $La_4Ti_3O_{12}$ and Mn^{4+}-doped composition with nominal formula $La_4(Ti_{2.998}Mn_{0.002})O_{12}$ were synthesized by the high-temperature solid state reaction. La_2O_3 (99.99%) was calcined in air at 1000 °C for 6 h prior to weighing, which was then immediately blended with stoichiometric amounts of TiO_2 (99.99%) and $MnCO_3$ (99.99%) after cooling to room temperature. The timely weighing of La_2O_3 was found to be necessary to avoid the formation of La_2TiO_5 secondary phase. The chemicals were mixed thoroughly in a mortar which were then transferred to lid-covered corundum crucibles. The mixtures were firstly heated at 1400 °C for 6 h, then pulverized and compacted into pellets which were finally heated at 1420 °C for 10 h in air. The cooling rate from 1420 °C to 1000 °C was 10 °C/min, and then, it got naturally cooled within the furnace.

Characterization. The phase composition was identified by X-ray diffraction (XRD) using Cu K_α radiation on an X-ray diffractometer (XRD-6000, Shimadzu, Kyoto, Japan) with operating voltage and current of 40 kV and 30 mA, respectively. The diffuse reflectance spectra were measured by a scanning-type spectrophotometer (UV3600; Shimadzu, Kyoto, Japan) equipped with a $BaSO_4$-coated integrating sphere. Photoluminescence (PL) and PL excitation (PLE) spectra were measured using a monochromator (Acton SP2300; Princeton Instruments, Massachusetts, USA) and a photomultiplier tube (H10330A-75; Hamamatsu Photonics, Hamamatsu, Japan) with temperature controlled by closed-cycle helium cryostat (SHI-APD, DE-204SLFF). The temperature-dependent luminescence was measured using a custom-made setup consisting of a Xe lamp with 400 nm bandpass filter, a multichannel charge-coupled device spectrometer (QE65Pro; Ocean Optics, Dunedin, FL, USA) and a thermal stage (10033L; Hightech, Fukuoka, Japan). Liquid nitrogen was employed as the cooling agent. A 300 W Xe lamp with bandpass filters was used as an excitation source.

Computational details. The density functional theory (DFT) with Perdew–Burke–Ernzerhof (PBE) exchange-correlation functional[11] as implemented in the VASP code[12] is used to study the Mn^{4+} emission in $La_4Ti_3O_{12}$. The

interaction between ions and electrons was described by projector augmented wave method.[13] The kinetic energy cutoff of 400 eV was used for the plane-wave basis. Experimental lattice parameters of $La_4Ti_3O_{12}$ were used while the atomic positions were fully relaxed until the residual forces were less than 0.02 eV/Å. The ZPL of Mn^{4+} emission was calculated by

$$\Delta E_{ZPL} = E(1\mu_B) - E(3\mu_B) \qquad Eq.\ (1)$$

where $E(1\mu_B)$ and $E(3\mu_B)$ are the total energies of structurally relaxed low-spin ($1\mu_B$) and high-spin ($3\mu_B$) states of Mn^{4+}.

Moreover, the exchange charge model of crystal field[14] was used to calculate the energy levels of the Mn^{4+} ions in $La_4Ti_3O_{12}$ (C_{3i} site). The crystal structural data[15] were used to analyze the symmetry properties of the impurity ion site and generate a cluster consisting of more than 66000 ions (this is needed to ensure proper convergence of the crystal lattice sums needed for the calculations of the crystal field parameters). Details of the calculations as well as all relevant equations can be found in related references[5,16] and are not repeated for the sake of brevity.

3 Results and discussion

3.1 TiO_6 octahedron coordination in $La_4Ti_3O_{12}$

Figure 1 shows the XRD pattern of the as-prepared $La_4(Ti_{2.998}Mn_{0.002})O_{12}$. It well coincides with the reference (No. 01-074-2661). The effective ionic radius (r) of the 6-fold coordinated Ti^{4+} (r = 0.605 Å) is larger than that of Mn^{4+} (r = 0.530 Å), providing hosting sites for Mn^{4+}. Figure 2 illustrates a unit cell of $La_4Ti_3O_{12}$ (drawn by VESTA[17]). The compound crystalizes in a rhombohedral structure[18,15] (space group $R\bar{3}$, No. 148) with lattice constants $a = b$ = 5.561(3) Å, c = 26.24(1) Å, $\alpha = \beta = 90°$, $\gamma = 120°$. Ti^{4+} ions at two crystallographic sites forms weakly distorted $Ti(1)O_6$ as well as strongly-distorted $Ti(2)O_6$ octahedra, respectively[15]. The $Ti\text{-}O_{i\text{-}vi}$ distances in the $Ti(1)O_6$ octahedron are all equal to 1.964 Å, and the minor distortion is caused by the variation of the O-Ti(1)-O bond angles. In comparison, the severe distortion of $Ti(2)O_6$ octahedron is caused by the variation of Ti(2)-O bond lengths ($Ti\text{-}O_{i,\ v,\ vi}$ distance of 2.098 Å and $Ti\text{-}O_{ii,\ iii,\ iv}$ distance of 1.860 Å) as well as the variation of O-Ti(2)-O bond angles. Thus, compared with the O_h symmetry of an ideal octahedron, the point symmetry of the Ti(1) site is lowered to be C_{3i} (with the C_3 rotation axis being parallel to the c crystallographic axis) while the Ti(2) site holds the point symmetry

of C_3 without an inversion center.

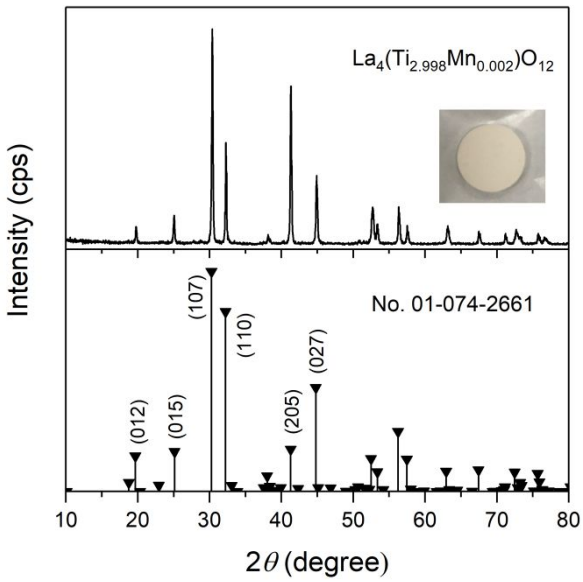

Figure 1 XRD pattern of the as-prepared $La_4(Ti_{2.998}Mn_{0.002})O_{12}$ (the insert shows digital image of the sample). The reference pattern (No. 01-074-2661) of $La_4Ti_3O_{12}$ was also given.

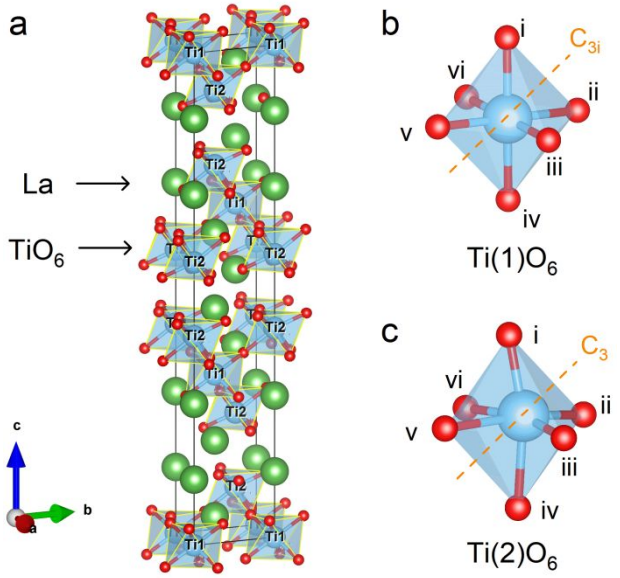

Figure 2 (a) Unit cell of $La_4Ti_3O_{12}$. There exist two crystallographic Ti^{4+} sites, forming slightly-distorted $Ti(1)O_6$ octahedron (b) and highly-distorted $Ti(2)O_6$ octahedron (c), respectively. The point group for the Ti(1) site is C_{3i} (the third-order axis is parallel to the *c*-axis, and goes through the center of the octahedron faces made by the (*i*, *ii*, *iii*) and (*iv*, *v*, *vi*) atoms), while the point group for the Ti(2) site is C_3 without inversion center.

The $Ti(1)O_6$ and $Ti(2)O_6$ octahedra are corner-linked, and the LaO_9 polyhedrons are either edge- or face-shared with these TiO_6 octahedra. The bond angle deviation in the $Ti(1)O_6$ octahedron is caused by the slight rotation of one O-Ti-O chain with the position of Ti(1) fixed at the center. By contrast, the distortion of $Ti(2)O_6$ can be interpreted

as Ti(2) moving from the inversion center approaching a facet of the octahedron. We use two indices, the mean quadratic elongation λ_{oct} and the bond angle variance (σ^2_{oct}), to evaluate the polyhedron distortion[6,19]:

$$\lambda_{oct} = \sum_{i=1}^{6} \frac{(l_i/l_0)^2}{6} \qquad Eq.\ (2)$$

$$\sigma^2_{oct} = \sum_{i=1}^{12} \frac{(\theta_i - \theta_0)^2}{12} \qquad Eq.\ (3)$$

In the equations, l_0 is the center-to-vertex distance for the undistorted octahedron equal in volume to the one in question, l_i is the ith bond length, θ_0 is the ideal bond angle 90° for a regular octahedron, and θ_i is the ith bond angle. Table 1 lists the calculated polyhedron distortion indices of the two Ti^{4+} sites in $La_4Ti_3O_{12}$ as well as the cation sites in several representative fluoride/oxyfluoride hosts (such as K_2SiF_6, Rb_2GeF_6, $Na_2WO_2F_4$, $Cs_2WO_2F_4$). The reported ZPL intensity with respect to the strongest phonon sideband intensity was also listed. The data in Table 1 suggests a more intense ZPL signal in the PL of the Ti(2) site-situated Mn^{4+} can be expected, considering the relatively large value of $\lambda_{oct}/\sigma^2_{oct}$ indices. Since the preparation was conducted at high temperature with long duration, we presume that the Mn^{4+} dopant has distributed in both Ti^{4+} sites.

Table 1 Space group, octahedron distortion indices and corresponding ZPL intensity in several typical hosts

Type	Compound/Site	Space group/Symmetry	λ_{oct}	σ^2_{oct}	ZPL intensity	ZPL/strongest phonon sideband intensity ratio (RT)
Oxide	$La_4Ti_3O_{12}$/Ti(1)	rhombohedral $R\bar{3}/C_{3i}$	1.00000	6.0025		
	$La_4Ti_3O_{12}$/Ti(2)	rhombohedral $R\bar{3}/C_3$	1.00370	56.9296		
Fluoride	K_2SiF_6/Si^{4+}	Cubic $Fm\bar{3}m/O_h$	1.00000	0.0000	Very weak	~0%[20]
	Rb_2GeF_6/Ge^{4+}	Hexagonal $P6_3mc/C_3$	1.00340	35.3698	Strong	~50%[21]
Oxyfluoride	$Na_2WO_2F_4/W^{6+}$	Orthorhombic $Pbcn/C_{2v}$	1.02485	78.5316	Very strong	~125%[6]
	$Cs_2WO_2F_4/W^{6+}$	Trigonal $P\bar{3}m1/C_{2v}$	1.00000	1.9044	Weak	~5%[22,23]

RT: Room temperature.

3.2 Spectroscopic properties of Mn^{4+} in $La_4Ti_3O_{12}$

Figure 3 shows the diffuse reflectance spectrum of the non-doped and the Mn^{4+}-doped $La_4Ti_3O_{12}$. Taking a direct-type band transition, the optical bandgap of $La_4Ti_3O_{12}$ was determined to be 3.90 eV from the $(\alpha h\nu)^{1/2}$–$h\nu$ plot, where α, h, and ν represent the Kubelka-Munk function, the Planck constant, and the frequency, respectively. The estimated bandgap is quite close to the reported value (3.95 eV)[24]. For the Mn^{4+}-doped sample, the broad absorption band in the near-UV to visible region originates from the spin-allowed $^4A_{2g}$ (^4F) → $^4T_{2g}$, $^4T_{1g}$ (^4F) transitions as well as the parity-allowed O^{2-} - Mn^{4+} charge transfer transition.

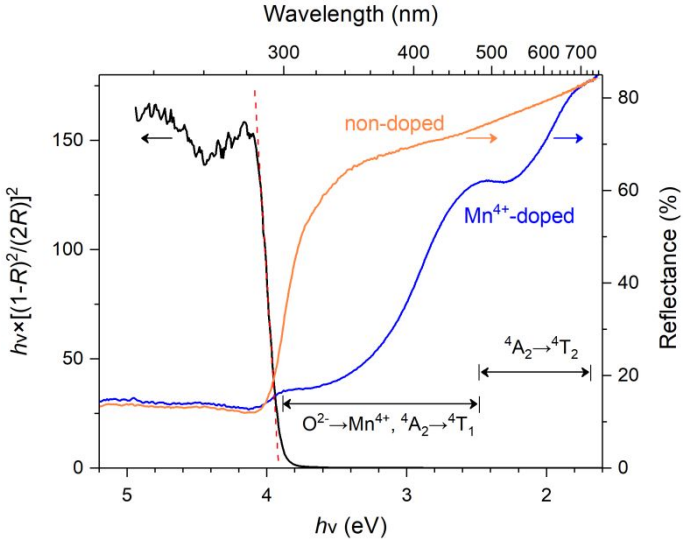

Figure 3 Diffuse reflectance spectrum and the Tauc plot of $La_4Ti_3O_{12}$. The optical bandgap is determined to be 3.90 eV, which is the intersection value of the tangent line (shown in red) with the x-axis.

Figure 4 exhibits the low-temperature photoluminescence excitation (PLE) and emission (PL) spectra of the $La_4(Ti_{2.998}Mn_{0.002})O_{12}$ phosphor at 20 K. The emission spectra consist of peaks A (706 nm, 14164 cm^{-1}), B (712 nm, 14045 cm^{-1}), C (715 nm, 13996 cm^{-1}), D (719 nm, 13912 cm^{-1}), E (724 nm, 13812 cm^{-1}), F (727 nm, 13755 cm^{-1}), G (732 nm, 13661 cm^{-1}), H (741 nm, 13495 cm^{-1}), I (748 nm, 13369 cm^{-1}), J (760 nm, 13158 cm^{-1}), K (770 nm, 12987 cm^{-1}). In principle, the PL should be composed of the ZPLs and the Stokes/anti-Stokes vibronic bands. The emissions at high frequency side of 14205 cm^{-1} (704 nm) were assigned to be anti-Stokes vibronic bands since the intensity gradually increased and then decreased with elevated temperatures. Upon temperature rise, the anti-Stokes emission is known to initially increase due to the population of higher vibronic states.[25] Generally, the anti-Stokes emissions on the high frequency side of ZPL are near mirror image of the Stokes phonon sideband emission. Emissions at low frequency side of 14205 cm^{-1} consist of ZPLs of the ^2E_g → $^4A_{2g}$ transition and the Stokes vibronic emissions originated from the *ungerade* vibrational modes (v_6, asymmetric bending; v_4, asymmetric bending; v_3, asymmetric

stretching) of the MnO_6 moieties in both Ti^{4+} sites. The ZPLs and Stokes emissions show distinct bands when excited by different energies (Figure 4a). The excitation by 400 nm induced the most intense emission at peak E (13812 cm^{-1}), while the 480 nm excitation resulted in the peak H (740 nm, 13514 cm^{-1}) as the strongest emission. This evidences that Mn^{4+} ions occupy both Ti^{4+} sites in $La_4Ti_3O_{12}$ experiencing distinct nephelauxetic effect and crystal filed splitting at each Ti^{4+} site.

To distinguish the origin of these emissions, the emission-selective PLE spectra were collected. As seen from Figure 4b, two sets of PLE spectra were respectively observed when monitoring the emission energies of 14164 cm^{-1} (706 nm, peak A), 14045 cm^{-1} (712 nm, peak B) and 13812 cm^{-1} (724 nm, Peak E), as well as those of 13514 cm^{-1} (740 nm, peak H) and 13158 cm^{-1} (760 nm, peak J). Each of the two sets of PLE spectra consists of either two or three discrete broad bands. We deduce that these emission peaks A to G originate from the $^2E_g \rightarrow {}^4A_{2g}$ transition of the Mn^{4+} seated at one crystallographic Ti^{4+} site, while the longer emission peaks H to K originate from the Mn^{4+} seated at another Ti^{4+} site. Our tentative assignment of the transitions responsible for the PLE bands were marked in the figure, including the *inter*configurational fully allowed (large change in dipole moment) $O^{2-} \rightarrow Mn^{4+}$ charge transfer (CT) transition together with the parity-forbidden but spin-allowed $^4A_{2g} \rightarrow {}^4T_{1g}$ and $^4A_{2g} \rightarrow {}^4T_{2g}$ transitions. According to the Tanabe-Sugano diagram for a d^3 ion, the spin-forbidden $^4A_{2g} \rightarrow {}^2T_{2g}$ transition should be also involved in the PLE, but the intensity should be quite low which is hard to identify and thus omitted. The $^4A_{2g} \rightarrow {}^4T_{2g}$ transition in both sets of PLEs is well distinguishable while the $^4A_{2g} \rightarrow {}^4T_{1g}$ transition is either distinguishable or overlapped with the $O^{2-} \rightarrow Mn^{4+}$ CT transitions (Figure 4b).

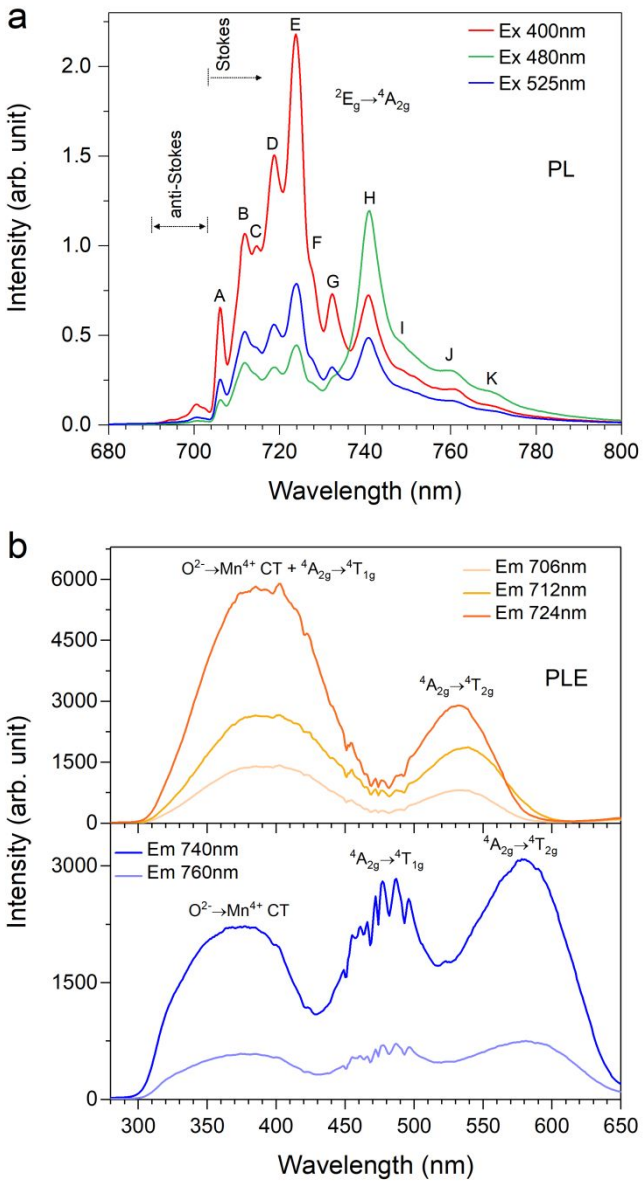

Figure 4 Photoluminescence (PL) and excitation (PLE) spectra of $La_4(Ti_{2.998}Mn_{0.002})O_{12}$ at 20 K: (a) PLs under excitation of 400 nm, 480 nm, and 525 nm; (b) PLEs monitoring various emission energies.

Moreover, we performed theoretical calculation of Mn^{4+} emission energy in both Ti^{4+} sites of $La_4Ti_3O_{12}$. Experimental lattice parameters of $La_4Ti_3O_{12}$ were used and the atomic positions were then fully relaxed. The Ti(1)-O bond length and two Ti(2)-O bond lengths in $La_4Ti_3O_{12}$ were calculated to be 1.962 Å, and 2.099 Å/1.871 Å, respectively, which are in good agreement with the experimental values of 1.964 Å, and 2.098 Å/1.860 Å. The substitutional Mn dopants on both Ti(1) and Ti(2) sites were studied. The $Mn_{Ti(1)}$-O and the two $Mn_{Ti(2)}$-O bond lengths were calculated to be 1.919Å, and 1.994 Å/1.862 Å, respectively. $Mn_{Ti(1)}$ was found to be more stable than $Mn_{Ti(2)}$ by 0.09 eV. Thus, the concentration of $Mn_{Ti(1)}$ could be higher than that of $Mn_{Ti(2)}$. Meanwhile,

crystallographically, the number of Ti(1) site is two times that of the Ti(2) site. Judging from the absorption wavelength of the diffuse reflection spectrum, the majority Mn^{4+} ions are seen to occupy the Ti(1) site. The calculated ZPLs of $Mn_{Ti(1)}$ and $Mn_{Ti(2)}$ emission using Eq. 1 are 0.92 eV and 0.89 eV, respectively. The PBE-calculated Mn^{4+} emission energy is expected to be significantly underestimated but has been shown to reproduce the experimental trend.[10] The Quantum Monte Carlo method, which is a more advanced many-body electronic structure method, has been shown to provide accurate Mn^{4+} emission energies in solids,[26] but would incur prohibitively high computational cost due to the relatively large cell of $La_4Ti_3O_{12}$. The ZPL/vibronic emission intensity ratio of $Mn_{Ti(2)}$ is likely larger, and the PL decay of $Mn_{Ti(2)}$ is likely faster than those of $Mn_{Ti(1)}$ due to the more distorted octahedral environment of $Mn_{Ti(2)}$.

Based on the theoretical calculation of ZPL energy of $Mn_{Ti(1)}$ and $Mn_{Ti(2)}$, we tentatively assign that the peaks A, B (energy difference of 119 cm^{-1}) are the split ZPLs of $Mn_{Ti(1)}$ and peak D/E, F, G are the split-ν_6, ν_4, and ν_3 vibronic phonon sideband emissions of $Mn_{Ti(1)}$. Meanwhile, the peaks H, I, J, and K are assigned as ZPL, ν_6, ν_4, and ν_3 vibronic phonon sideband emissions, respectively, from PL of $Mn_{Ti(2)}$. The origin for the peak C is unknown at present. It is worth to note that the full-width at half-maximum of the peak H is broader than those of ZPL peaks A/B, which indicates the ZPL splitting of $Mn_{Ti(2)}$. With such assignment, the ZPL/ν_6 intensity ratio is about 50% for $Mn_{Ti(1)}$, and 200% for $Mn_{Ti(2)}$. This situation is consistent with the fact that $Mn_{Ti(1)}O_6$ has the inversion symmetry whereas $Mn_{Ti(2)}$ does not. The breaking of inversion center symmetry relaxes the parity-/spin-selection rule, leading to a higher transition probability and thus a higher ZPL/ν_6 intensity ratio. Our assignment of the emission peaks A/B and H as the split ZPLs also coincides with previous observations that (1) the split ZPLs show different intensities (due to different transition probabilities) with respect to phonon sideband emission, (2) the energy difference of the split ZPLs is $\leq$ 100 cm^{-1}, and (3) the full-width at half-maximum of ZPL peaks is much smaller than the vibronic emission peaks.

Two and five split ZPLs have been reported for the PL of $K_2TiF_6:Mn^{4+}$ (one kind of crystallographic Ti^{4+} site) by Chen et al.[27] and PL of $Na_3GaF_6:Mn^{4+}$ (three kinds of crystallographic Ga^{3+} sites) by Jüstel et al.[28], respectively. When the local octahedron symmetry is reduced from O_h, the Mn^{4+} energy levels (such as $^4T_{1g}$ and $^4T_{2g}$) start to split according to group theory, and when spin-orbit coupling is also considered, the ^2E_g and $^4A_{2g}$ states each split further into two sublevels.[28] Then, the emission from the $^2E_g \rightarrow {}^4A_{2g}$ transition of one crystallographic Mn^{4+} results in two ZPLs. A scheme of Mn^{4+} energy level splitting under the combined effects of site symmetry lowering and the spin-orbit interaction was given in Figure 5, referring to the energy level splitting of Mn^{4+} in K_2TiF_6 host[27]. That is to say,

the splitting of ZPL occurred in both $Mn_{Ti(1)}$ and $Mn_{Ti(2)}$ due to site symmetry lowering and spin-orbit interaction, but the fine structure of splitting is more clarified in the PLs of $Mn_{Ti(1)}$.

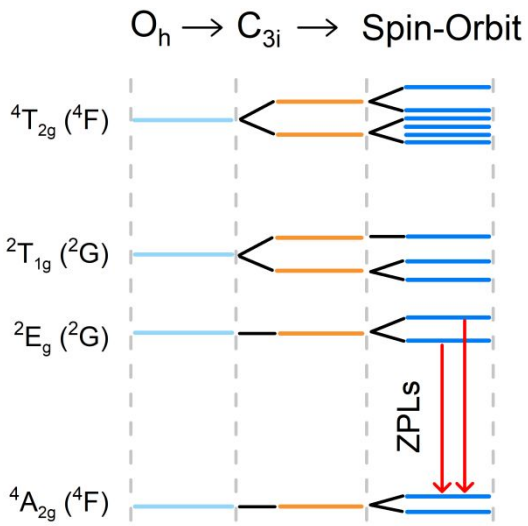

Figure 5 Scheme of Mn^{4+} energy level splitting under combined effects of site symmetry lowering (from O_h to C_{3i} as a case) and spin-orbit interaction, resulting in bi-ZPL emission.

The Mn^{4+} $^2E_g \rightarrow {}^4A_{2g}$ transition energy is affected by nephelauxetic effect and has weak dependence on the crystal field strength (the emitting ^2E_g state is nearly flat in Tanabe-Sugano diagram for a d^3 ion). The degree of the nephelauxetic effect is related to the wave functions' overlap between Mn-3d and ligand-2p. The greater the overlap is (which means more effective sharing of electrons between Mn^{4+} and its nearest ligands), the stronger the covalent bond forms and the more pronounced nephelauxetic effect is.[29] Generally, the greater is the octahedral distortion, the smaller is the overlap between the Mn-3d and O-2p wave functions and the higher is the energy position of the ^2E_g state.[8,9,10] Srivastava and Brik et al. have presented how the "Mn^{4+}-O^{2-}" covalent mixing is influenced by connectivity of the octahedral moieties and deviation of O-Mn-O bond angle from 90°, after comparatively examining the cases in which octahedra either share corners as in perovskite/pyrochlore, or edges and faces as in α-$LiAlO_2$, $Sr_4Al_{14}O_{25}$ and $CaAl_{12}O_{19}$.[8,9] A highly symmetrical octahedral moiety increases "Mn^{4+}-O^{2-}" bonding covalence and lowers the $^2E_g \rightarrow {}^4A_{2g}$ transition energy. It may be expected that the Mn-O bonding covalence in $Ti(1)O_6$ with shorter $Mn_{Ti(1)}$-O bond lengths is higher than that in $Ti(2)O_6$ with longer average $Mn_{Ti(2)}$-O bond length, leading to lower ZPL energy of $Mn_{Ti(1)}$. This analysis, however, contradicts against the calculated trend that the ZPL of $Mn_{Ti(1)}$ (0.92 eV) is slightly higher than the ZPL of $Mn_{Ti(2)}$ (0.89 eV). It is worthwhile to mention that three chemical bonds in the $Ti(2)O_6$ octahedron are considerably shorter than in the $Ti(1)O_6$ octahedron (1.860 Å *vs.* 1.964 Å, respectively), whereas the three remaining chemical bonds in the $Ti(2)O_6$ octahedron are considerably longer than in the $Ti(1)O_6$ octahedron

(2.098 Å *vs.* 1.964 Å, respectively). So, in this particular host interplay of the chemical bond length variation and angular distortion appears to be important for the positions of the ZPL lines originating from the Mn^{4+} ions located at different crystallographic sites.

It is seen that under near-UV irradiation (400 nm), the ZPLs, instead of phonon sideband, contribute to a large extent (in case of $Mn_{Ti(1)}$) or even dominate the emission (in case of $Mn_{Ti(2)}$). The $^2E_g \rightarrow {}^4A_{2g}$ transition is both parity- and spin-forbidden, which explains the weak ZPL in most of Mn^{4+}-doped phosphor (for example, the commercial $K_2SiF_6:Mn^{4+}$). The emission gains intensity since the parity selection rule can be partly relaxed by coupling with asymmetric vibrations that induce odd-parity crystal field components. For a MnO_6 moiety that lacks an inversion center, the parity selection rule can also be relaxed by odd-parity crystal field components that admix odd-parity wavefunctions into the Mn^{4+} d wavefunction. Thus, the distortion of both Ti^{4+} site favors the relaxation of the parity selection rule and permit intense ZPL emission. Moreover, considering the relatively long decay of Mn^{4+} $^2E_g \rightarrow {}^4A_{2g}$ transition, it would be also interesting to compare the lifetime (transition rate) of the ZPL emission and the vibronic emission.

The crystal field strength and the Racah parameters of Mn^{4+} in both Ti^{4+} sites were compared. The peak energy of the $^4A_{2g} \rightarrow {}^4T_{2g}$ transition band was taken to calculate the crystal field strength ($10Dq$) following Eq. 4:

$$10Dq = E\left({}^4T_{2g} - {}^4A_{2g}\right) \qquad Eq.\ (4)$$

and the Racah parameter B and C are calculated following Eqs. 5 and 6:

$$\frac{B}{Dq} = \frac{\left(\frac{\Delta E}{Dq}\right)^2 - 10\frac{\Delta E}{Dq}}{15\left(\frac{\Delta E}{Dq} - 8\right)} \qquad Eq.\ (5)$$

$$3.05C = E\left({}^2E_g - {}^4A_{2g}\right) - 7.9B + \frac{1.8B^2}{Dq} \qquad Eq.\ (6)$$

where ΔE is the energy difference between the $^4T_{2g}$ and $^4T_{1g}$ energy levels.

The peak wavelength of each transition in the PLE/PL band was used as $E(^4T_{1g})$, $E(^4T_{2g})$, or $E(^2E_g)$, respectively. The ZPL energy of the Mn^{4+} $^4A_{2g} \rightarrow {}^4T_{2g}$ transition is practically difficult to determine due to (1) the occurrence of different phonon-assisted transitions, and (2) energy splitting of the $^4T_{2g}$ level by the low-symmetry crystal field

components and the spin-orbit interaction. Meanwhile, the PLE spectrum monitored for the 724 nm emission was deconvoluted into three Gaussian components to identify the $O^{2-}\rightarrow Mn^{4+}$ CT, the $^4A_{2g} \rightarrow {}^4T_{1g}$ and the $^4A_{2g} \rightarrow {}^4T_{2g}$ transition energies (given in Figure 6).

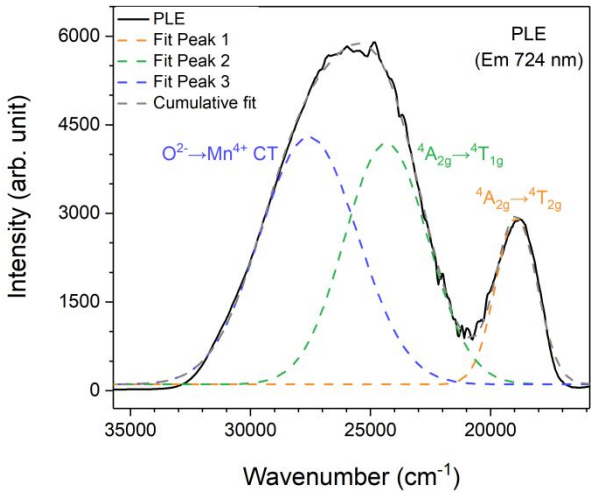

Figure 6 Deconvolution of the PLE spectra monitored for the 724 nm emission into three Gaussian components (T = 20 K) to identify the different transition energies.

If the energies of the ^2E_g, $^4T_{2g}$, and $^4T_{1g}$ for $Mn_{Ti(1)}$ are taken from our measurement at 20 K to be 14164, 18797, and 24358 cm^{-1}, and these for $Mn_{Ti(2)}$ to be 13498, 17271, and 22727 cm^{-1}, respectively, we can determine the crystal field parameter Dq and the Racah parameters B and C for Mn^{4+} ions: substituting Ti(1), Dq = 1880 cm^{-1}, B = 518 cm^{-1}, C = 3387 cm^{-1}, and substituting Ti(2), Dq = 1727 cm^{-1}, B = 514 cm^{-1}, C = 3184 cm^{-1}. The estimated Dq value is similar with those reported for Mn^{4+} in $SrTiO_3$ (Dq = 1821 cm^{-1}, B = 735 cm^{-1}, C = 2812 cm^{-1}) and $BaTiO_3$ (Dq = 1780 cm^{-1}, B = 738 cm^{-1}, C = 2820 cm^{-1}) summarized by Brik et al.[30] However, the calculated Racah parameter B derivates clearly from that reported for Mn^{4+} in $SrTiO_3$ and $BaTiO_3$, and is much smaller than the reported lower limit of ~550-600 cm^{-1}. The PLE spectrum monitoring for the 760 nm emission may be distributed by some unknown reasons such as energy transfer from $Mn_{Ti(1)}$ to $Mn_{Ti(2)}$, impurity absorption, saturation, *etc*., and it becomes difficult to determine precise $^4T_{2g}$ and $^4T_{1g}$ position for $Mn_{Ti(2)}$. Thus, the Racah parameters calculated for $Mn_{Ti(2)}$ is not necessarily highly reliable.

Besides, as indicated by the aforementioned DFT calculation, the $Mn_{Ti(1)}$-O and the two $Mn_{Ti(2)}$-O bond lengths have been calculated to be 1.919 Å, 1.994 Å/1.862 Å, respectively. Thus, $Mn_{Ti(2)}$-O has a slight longer average bond length (1.928 Å) than that of $Mn_{Ti(1)}$-O. Srivastava and Brik[31] summarized that the $10Dq$ depends on the metal-ligand distance with a relationship of $10Dq = K/R^n$, where K is a constant and n is close to five. Following this trend, the

crystalline field strength (measured by $10Dq$) would decrease with increasing Mn–O bond length. Present assignment indicated the $Mn_{Ti(1)}$ experiences a slight larger $10Dq$ than $Mn_{Ti(2)}$, which coincides with the above trend.

Table 2 The crystal filed strength and Racah parameters calculated for Mn^{4+} in both Ti^{4+} sites

	O-Mn CT (cm^{-1})	$10Dq$ (cm^{-1})	ΔE ($^4T_{1g}$-$^4T_{2g}$) (cm^{-1})	^2E_g (cm^{-1})	B (cm^{-1})	C (cm^{-1})	β_1
$Mn_{Ti(1)}$	27581	18797	5561	14164	518	3387	0.82
$Mn_{Ti(2)}$	26734	17271	3476	13498	514	3184	0.86

As shown in Eq. 7, the parameter β_1 was introduced by Brik and Srivastava[32] in the spectroscopy of d^3 ions to connect the energy of the $^2E_g \rightarrow {}^4A_{2g}$ transition with the Racah parameters B and C (B_0 and C_0 are 1160 cm^{-1} and 4303 cm^{-1}, respectively, and the subscript "0" refers to the values of the Racah parameters of free Mn^{4+} ion). β_1 quantifies the nephelauxetic effect which simultaneously take into account the reduction in both B and C parameters. The β_1 values were calculated for Mn^{4+} in both Ti^{4+} sites using Eq. 7. The energy of the ^2E_g level predicted from the linear function $E(^2E_g \rightarrow {}^4A_{2g}) = -142.83 + 15544.022\beta_1$ was 13924 cm^{-1} and 13264 cm^{-1} for $Mn_{Ti(1)}$ and $Mn_{Ti(2)}$, respectively. The differences from the experimental results (ZPL for $Mn_{Ti(1)}$, 14045 cm^{-1}, for $Mn_{Ti(2)}$, 13494 cm^{-1}) are 121 cm^{-1}, and 230 cm^{-1}, and are within the reported deviation range ($\sigma = 365$ cm^{-1}). This deviation can be caused by the fact that the Mn^{4+} $^4A_{2g} \rightarrow {}^4T_{2g}/{}^4T_{1g}$ transition is accompanied by the vibronic progressions and the ZPL position cannot be always determined unambiguously.

$$\beta_1 = \sqrt{\left(\frac{B}{B_0}\right)^2 + \left(\frac{C}{C_0}\right)^2} \qquad Eq.\ (7)$$

Since Mn^{4+} ions are seen to be mainly seated in the Ti(1) site, the theoretical calculation was thus paid attention to $Mn_{Ti(1)}$ with point symmetry of C_{3i}. The non-zero parameters of crystal field calculated by the exchange charge model are listed in Table 3. The values of the Racah parameters B and C, which were chosen from the best agreement with experimental data, are also given in the same Table. The crystal field splitting of all 8 LS terms of the Mn^{4+} ion was calculated by diagonalizing the crystal field Hamiltonian with all crystal field parameters. The lowest calculated energy levels, which are located in the spectral range corresponding to the experimental excitation/emission spectra, are listed in Table 4. There is good agreement between these calculated energy levels and corresponding experimental data listed in Table 2.

Table 3 Non-zero crystal field parameters B_p^k (Stevens normalization) and Racah parameters *B*, *C* (all in cm^{-1}) for Mn^{4+} ion in $La_4Ti_3O_{12}$ (C_{3i} site). The values of the exchange charge model parameter *G* are also given.

	Ti site (C_{3i})
B_2^0	-1550
B_4^{-3}	-79531
B_4^0	-3065
B_4^3	51588
G	6.65
B	518
C	3395

Table 4 Calculated energy levels (all in cm^{-1}) for Mn^{4+} ion in $La_4Ti_3O_{12}$ (C_{3i} site). The orbital doublet states are denoted with an asterisk.

"Parent" O_h states	C_{3i} group notation	Energy, calculated	Energy, observed
$^4A_2$ (^4F)	^4A_g	0	
^2E (^2G)	$\{^2E_g(1) + {}^2E_g(2)\}$	14163*	14164
$^2T_1$ (^2G)	$^2A_g + \{^2E_g(1) + {}^2E_g(2)\}$	14402, 14658*	
$^4T_2$ (^4F)	$^4A_g + \{^4E_g(1) + {}^4E_g(2)\}$	18590, 18866*	18797
$^2T_2$ (^2G)	$\{^2E_g(1) + {}^2E_g(2)\} + {}^2A_g$	22305*, 22438	
$^4T_1$ (^4F)	$^4A_g + \{^4E_g(1) + {}^4E_g(2)\}$	24188*, 24624	24358
$^4T_1$ (^4P)	$^4A_g + \{^4E_g(1) + {}^4E_g(2)\}$	38917, 40131*	

3.3 Thermal quenching of Mn^{4+} luminescence in $La_4Ti_3O_{12}$

The Mn^{4+} luminescence showed severe quenching under thermal effect in $La_4Ti_3O_{12}$. The quenching was studied in the range of 80-280 K under excitation of 400 nm, 510 nm, and 570 nm, respectively, as shown in Figure 7. Under λ_{ex} = 400 nm, the integral intensity firstly increased in the temperature range of 80 K to 120 K due to the enhancement of anti-Stokes emission and then started to decrease when T > 120 K due to increased nonradiative transition rate. Whereas, the integral emission intensity under λ_{ex} = 510 nm or 570 nm encountered steep decrease when T > 80 K. The temperature dependence of the integral luminescence intensity was fitted by using Eq. 8, to get the activation barrier for quenching:

$$\frac{I(T)}{I_0} = \frac{1}{1 + \Gamma_v/\Gamma_0 \exp(-E_a/kT)} \qquad Eq.(8)$$

where $I(T)$ is the integrated intensity at temperature T, I_0 is the integrated intensity at low temperature (here the intensity at 80 K was used as I_0), Γ_v is the radiative decay rate, Γ_0 is the attempt rate of the nonradiative process (Γ_v/Γ_0 forms a rate constant), E_a is the activation energy for quenching, k is Boltzmann constant (8.6173×10^{-5} eV K^{-1}) and T is temperature (in Kelvin). The estimated E_a values are 0.20(1) eV, 0.14(1) eV, and 0.12(1) eV, and the quenching temperature ($T_{50\%}$, the temperature at which the intensity drops to be half of the initial value) are 182 K, 166 K, and 158 K, for λ_{ex} = 400 nm, 510 nm, and 570 nm, respectively. Therefore, the emission at longer wavelength is seen to get thermally quenched more severe than those at shorter wavelength. One possible explanation is that $Mn_{Ti(1)}$ and $Mn_{Ti(2)}$ experience different quenching barriers. To verify, the PLs under 400 nm excitation were integrated in two spectral regions, the region 1 (from 705 nm to 728 nm) and region 2 (from 734 nm to 780 nm). The integral intensity of the two PL regions against temperature were shown in Figure 8. It's clear that the integral intensity in region 2 quenched faster than that of the region 1. This can be caused by the fact that $Mn_{Ti(1)}$ and $Mn_{Ti(2)}$ luminescence exhibit different thermal activation barriers considering the differences of $^4T_{2g}$ energy and $O^{2-} \rightarrow Mn^{4+}$ CT energy of $Mn_{Ti(1)}$ and $Mn_{Ti(2)}$. As seen from Table 2, Mn^{4+} in Ti(1) site exhibited a higher $^4T_{2g}$ energy and a higher CT state than that in Ti(2) site; this follows the trend that $T_{50\%}$ increases with the energy of the $^4T_{2g}$ state.

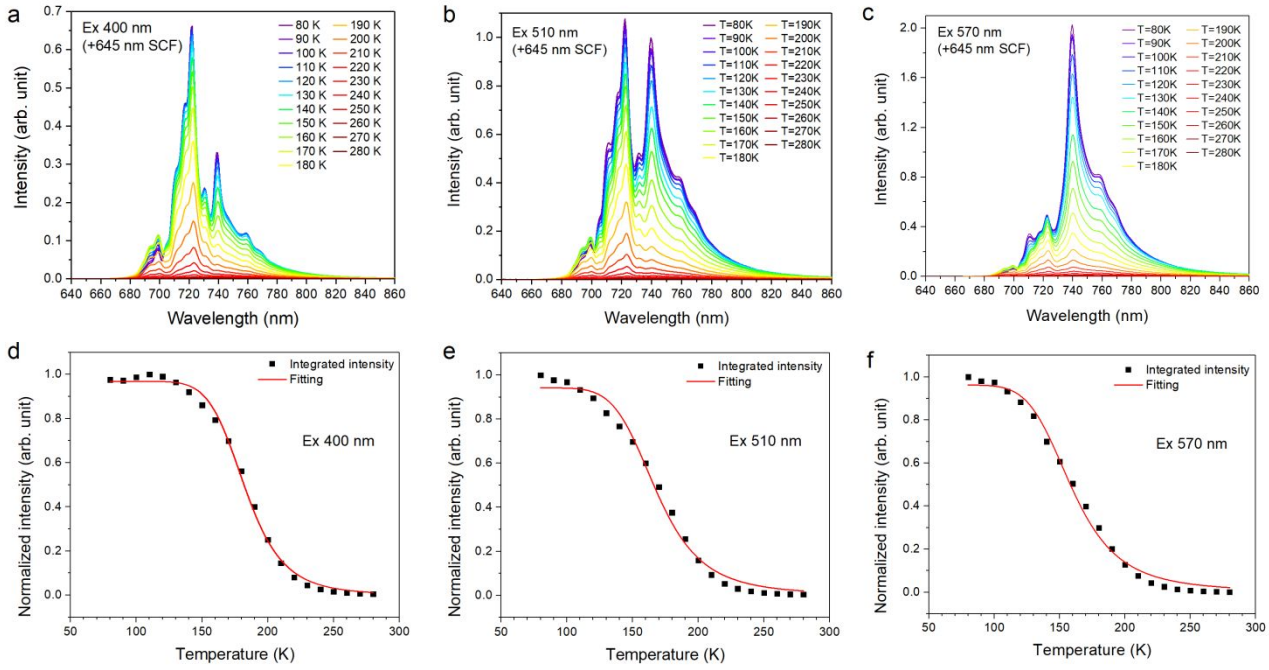

Figure 7 PLs of $La_4Ti_{2.998}O_{12}$:$0.002Mn^{4+}$ at different temperatures (from 80 K to 280 K) under excitation of 400 nm (a), 510 nm (b), and 570 nm (c). Temperature dependences of the integral luminescence intensity (from 680 nm to 800 nm) were fitted by the Fermi-Dirac function and shown in (d), (e), (f), respectively. SCF, Short Cut Filter.

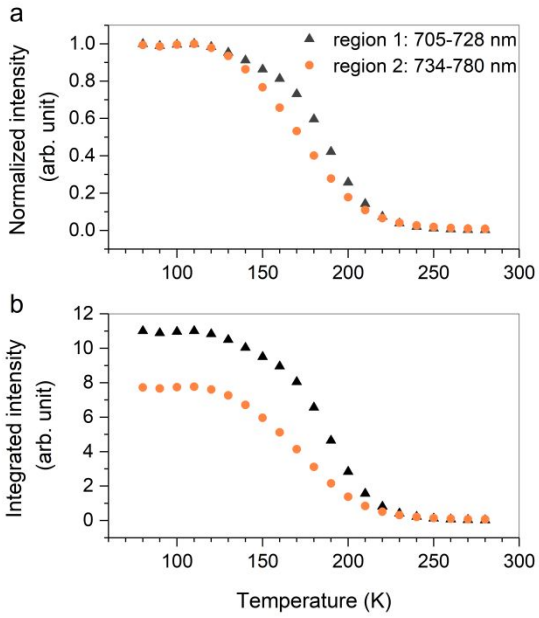

Figure 8 Evolution of the (a) normalized intensity and (b) integral intensity of the two PL regions (region 1: 605-728 nm, region 2: 734-780 nm; excitation 400 nm) against temperature.

Several mechanisms have been used to explain the Mn^{4+} luminescence thermal quenching. The first one is thermal-assisted crossover, either from the emitting ^2E_g state to the Franck-Condon shifted $^4T_{2g}$ level or to the low-lying $O^{2-} – Mn^{4+}$ CT state and finally non-radiative relaxation to the $^4A_{2g}$ level. This model have been considered as a main quenching mechanism for most Mn^{4+} doped fluoride and oxide phosphors.[33,34] Recently, Senden et al.[35] discussed four possible quenching process for the Mn^{4+} doped fluoride phosphors, including the multi-phonon relaxation, the thermal assisted photoionization of Mn^{4+} ^2E_g state to the host conduction band, and thermally activated crossover *via* the charge transfer state or Mn^{4+} $^4T_{2g}$ state; a clear trend between the $T_{50\%}$ (at which temperature the luminescence intensity decreases to be half) and the energy of the $^4T_{2g}$ state was seen in a series of fluoride phosphors, which demonstrated the crossover quenching from the $^4T_{2g}$ state. However, there is still a possibility of thermally activated crossover quenching *via* the charge transfer state in some Mn^{4+}-doped oxides, which have lower charge transfer energy. The CT is attributed to the transition from O^{2-}-Mn^{4+} state to O^{-}-Mn^{3+} state. The O^{-}-Mn^{3+} state can be interpreted as that Mn^{4+} leaves a hole to the valence band and changes into Mn^{3+}. Although the absorption energy of the CT state is higher than that of $^4A_{2g}\rightarrow{}^4T_{2g}$, it is known that the CT state has larger configurational offset. Thus, the bottom of CT state can be located below than that of $^4T_{2g}$ in some oxide hosts. In this situation, the crossover *via* the CT state becomes a dominant process with the excited Mn^{4+}:^2E_g state being thermally excited to the O^{-}-Mn^{3+} CT state.

Inspired by these studies, a schematic illustration, including the thermal crossover from the $^4T_{2g}$ state and CT

state, was drawn in Figure 9, to explain the thermal quenching of $La_4Ti_3O_{12}:Mn^{4+}$ luminescence. For Mn^{4+} luminescence quenching in fluoride, the quenching mechanism should be the crossover relaxation from ^2E to $^4T_2$ state, since the F^- to $Mn^{4+/3+}$ CT has a quite high energy and the F^- 2p locates at a lower binding energy level. While in $La_4Ti_3O_{12}$, the O^{2-} to $Mn^{4+/3+}$ charge transfer indeed occurred at quite low energy and the crossover quenching via the charge transfer (hole transfer) is a possible quenching mechanism. Further photocurrent measurement under different charging wavelengths and high temperatures would give evidence for or exclude the hole-type quenching mechanism.

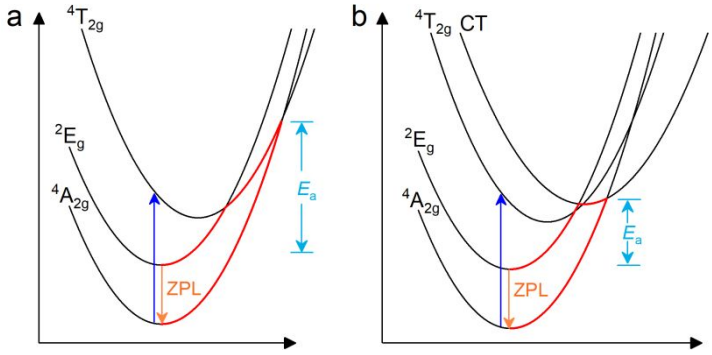

Figure 9 The proposed thermal quenching mechanisms for Mn^{4+} luminescence in $La_4Ti_3O_{12}$: (a) thermal assisted crossover *via* the $^4T_{2g}$ state and (b) thermal assisted crossover *via* the charge transfer (CT) state. The red lines indicate the non-radiative relaxation process in each model.

4 Conclusions

We studied the spectroscopic property of Mn^{4+} in the double perovskite $La_4Ti_3O_{12}$, which accommodates two kinds of TiO_6 octahedra including the slightly-distorted $Ti(1)O_6$ and the highly-distorted $Ti(2)O_6$. The distortion of $Ti(1)O_6$ is caused by the variation of the O-Ti(1)-O bond angles, while the severe distortion of $Ti(2)O_6$ is caused by not only the variation of Ti(2)-O bond lengths but also the variation of O-Ti(2)-O bond angles. Mn^{4+} in Ti(1) site seated at the center of inversion with a reduced symmetry of C_{3i}, while Mn^{4+} in Ti(2) site lost the inversion center and has a reduced symmetry of C_3. Spectroscopic studies revealed that Mn^{4+} got distributed in both Ti^{4+} sites and exhibited an ultrabroadband emission consisting of as many as eleven discrete peaks. The octahedral distortion has an influence on the stabilization of Mn^{4+} and the DFT calculation suggested that $Mn_{Ti(1)}$ is be more stable than $Mn_{Ti(2)}$ by 0.09 eV. The concentration of $Mn_{Ti(1)}$ is higher than that of $Mn_{Ti(2)}$ as evidenced by the diffuse reflectance spectrum. The Mn-O covalent interaction and the energy of the Mn^{4+} $^2E_g \rightarrow {}^4A_{2g}$ transition were greatly influenced by the MnO_6 octahedron distortion, as revealed by the site-selective PLE/PL study. Clear splitting of the ZPLs and the vibronic phonon sideband emissions was observed due to the site symmetry lowering and the spin-orbit interaction. The $Mn_{Ti(2)}$

showed a more intense zero phonon line emission with respect to the vibronic emission due to a more severe MnO_6 distortion. The Mn^{4+} $^2E_g \rightarrow {}^4A_{2g}$ transition emission exhibited severe thermal quenching in $La_4Ti_3O_{12}$. The lower-energy emission from $Mn_{Ti(2)}$ got thermally quenched more severe than the higher-energy emission from $Mn_{Ti(1)}$, due to the different thermal activation barriers of the $Mn_{Ti(1)}$ and $Mn_{Ti(2)}$ luminescence. Mn^{4+} in Ti(1) site exhibited a higher $^4T_{2g}$ energy which follows the trend that $T_{50\%}$ increases with the energy of the $^4T_{2g}$ state. The severe thermal quenching can be explained by the low-lying $^4T_{2g}$ level as well as the low-lying O^{2-} to $Mn^{4+/3+}$ charge transfer state.

Acknowledgements

This work is supported by the JSPS KAKENHI (Grant No. 16K05934). H. Ji also thanks the National Natural Science Foundation of China (No. 51902291) and the Postdoctoral Research Sponsorship in Henan Province (No. 19030025). D. Chen also thanks the China Postdoctoral Science Foundation (Nos. 2019M652574 and 2019M652570). M.-H. Du was supported by the U. S. Department of Energy, Office of Science, Basic Energy Sciences, Materials Sciences and Engineering Division.

ORCID

Haipeng Ji, http://orcid.org/0000-0003-2585-5665

Jumpei Ueda, http://orci d.org/0000-0002-7013-9708

Mikhail G. Brik, http://orcid.org/0000-0003-2841-2763

Mao-Hua Du, http://orcid.org/0000-0001-8796-167X

Deliang Chen, http://orcid.org/0000-0002-2076-8733

Setsuhisa Tanabe, http://orci d.org/0000-0002-7620-0119

References

1 H. F. Sijbom, R. Verstraete, J. J. Joos, D. Poelman and P. F. Smet, K_2SiF_6:Mn^{4+} as a red phosphor for displays and warm-white LEDs: a review of properties and perspectives, *Opt. Mater. Express*, 2017, **7**, 3332–3365.

2 Q. Zhou, L. Dolgov, A. M. Srivastava, L. Zhou, Z. Wang, J. Shi, M. D. Dramićanin, M. G. Brik and M. Wu, Mn^{2+} and Mn^{4+} red phosphors: synthesis, luminescence and applications in WLEDs. A review, *J. Mater. Chem. C*, 2018, **6**, 2652–2671.

3 T. Lesniewski, S. Mahlik, M. Grinberg and R.-S. Liu, Temperature effect on the emission spectra of narrow band Mn^{4+} phosphors for application in LEDs, *Phys. Chem. Chem. Phys.*, 2017, **19**, 32505–32513.

4 X. Ding, Q. Wang and Y. Wang, Rare-earth-free red-emitting $K_2Ge_4O_9$:Mn^{4+} phosphor excited by blue light for warm white LEDs, *Phys. Chem. Chem. Phys.*, 2016, **18**, 8088–8097.

5 A. M. Srivastava and M. G. Brik, The nature of Mn^{4+} luminescence in the orthorhombic perovskite, $GdAlO_3$, *Opt. Mater.*, 2017, **63**, 207–212.

6 T. Hu, H. Lin, Y. Cheng, Q. Huang, J. Xu, Y. Gao, J. Wang and Y. Wang, A highly-distorted octahedron with a C_{2v} group symmetry inducing an ultra-intense zero phonon line in Mn^{4+}-activated oxyfluoride $Na_2WO_2F_4$, *J. Mater. Chem. C*, 2017, **5**, 10524–10532.

7 M. G. Brik, W. W. Beers, W. Cohen, S. A. Payne, N. J. Cherepy, M. Piasecki and A. M. Srivastava, On the Mn^{4+} R-line emission intensity and its tunability in solids, *Opt. Mater.*, 2019, **91**, 338–343.

8 A. M. Srivastava, M. G. Brik, H. A. Comanzo, W. W. Beers, W. E. Cohen and T. Pocock, Spectroscopy of Mn^{4+} in double perovskites, La_2LiSbO_6 and La_2MgTiO_6: Deep red photon generators for agriculture LEDs, *ECS J. Solid State Sci. Technol.*, 2018, **7**, R3158–R3162.

9 A. M. Srivastava and M. G. Brik, Interpretation of the spectroscopic properties of α-$LiAlO_2$:Mn^{4+}, *ECS J. Solid State Sci. Technol.*, 2018, **7**, R3012–R3015.

10 M. H. Du, Chemical trends of Mn^{4+} emission in solids, *J. Mater. Chem. C*, 2014, **2**, 2475–2481.

11 J. P. Perdew, K. Burke and M. Ernzerhof, Generalized gradient approximation made simple, *Phys. Rev. Lett.*, 1996, **77**, 3865–3868.

12 G. Kresse and J. Furthmüller, Efficiency of ab-initio total energy calculations for metals and semiconductors using a plane-wave basis set, *Comput. Mater. Sci.*, 1996, **6**, 15–50.

13 G. Kresse and D. Joubert, From ultrasoft pseudopotentials to the projector augmented-wave method, *Phys. Rev. B*, 1999, **59**, 1758–1775.

14 B. Z. MALKIN, in *Spectroscopy of Solids Containing Rare Earth Ions*, eds. A. A. KAPLYANSKII and R. M. B. T.-M. P. in C. M. S. MACFARLANE, Elsevier, 1987, 21, 13–50.

15 P. Konstantinov, K. Krezhov, E. Sváb, G. Mészáros and G. Török, Neutron powder diffraction refinement of the crystal structure of $La_4Ti_3O_{12}$, *Phys. B Condens. Matter*, 2000, **276–278**, 260–261.

16 A. M. Srivastava, S. J. Camardello and M. G. Brik, Luminescence of Mn^{4+} in the orthorhombic perovskite, $LaGaO_3$, *J. Lumin.*, 2017, **183**, 437–441.

17 K. Momma and F. Izumi, VESTA 3 for three-dimensional visualization of crystal, volumetric and morphology data, *J. Appl. Crystallogr.*, 2011, **44**, 1272–1276.

18 G. Trolliard, N. Harre, D. Mercurio and B. Frit, Cation-deficient perovskite-related $(Ba,La)_nTi_{n-\delta}O_{3n}$ ($n \geq 4\delta$)

microphases in the $La_4Ti_3O_{12}$–$BaTiO_3$ System: An HRTEM approach, *J. Solid State Chem.*, 1999, **145**, 678–693.

19 M. E. Fleet, Distortion parameters for coordination polyhedra, *Mineral. Mag.*, 1976, **40**, 531–533.

20 A. G. Paulusz, Efficient Mn(IV) emission in fluorine coordination, *J. Electrochem. Soc.*, 1973, **120**, 942–947.

21 S. Sakurai, T. Nakamura and S. Adachi, Synthesis and properties of Rb_2GeF_6:Mn^{4+} red-emitting phosphors, *Jpn. J. Appl. Phys.*, 2018, **57**, 22601.

22 P. Cai, L. Qin, C. Chen, J. Wang and H. J. Seo, Luminescence, energy transfer and optical thermometry of a novel narrow red emitting phosphor: $Cs_2WO_2F_4$:Mn^{4+}, *Dalt. Trans.*, 2017, **46**, 14331–14340.

23 P. Cai, X. Wang and H. J. Seo, Excitation power dependent optical temperature behaviors in Mn^{4+} doped oxyfluoride $Na_2WO_2F_4$, *Phys. Chem. Chem. Phys.*, 2018, **20**, 2028–2035.

24 Y. Miseki, H. Kato and A. Kudo, Water splitting into H_2 and O_2 over niobate and titanate photocatalysts with (111) plane-type layered perovskite structure, *Energy Environ. Sci.*, 2009, **2**, 306–314.

25 H. Ji, J. Xu, K. Asami, J. Ueda, M. G. Brik and S. Tanabe, Local coordination, electronic structure, and thermal quenching of Ce^{3+} in isostructural Sr_2GdAlO_5 and Sr_3AlO_4F phosphors, *J. Am. Ceram. Soc.*, 2019, **102**, 1316–1328.

26 K. Saritas, W. Ming, M.-H. Du and F. A. Reboredo, Excitation energies of localized correlated defects via quantum monte carlo: A case study of Mn^{4+}-doped phosphors, *J. Phys. Chem. Lett.*, 2019, **10**, 67–74.

27 H. Zhu, C. C. Lin, W. Luo, S. Shu, Z. Liu, Y. Liu, J. Kong, E. Ma, Y. Cao, R.-S. Liu and X. Chen, Highly efficient non-rare-earth red emitting phosphor for warm white light-emitting diodes, *Nat. Commun.*, 2014, **5**, 4312.

28 D. Böhnisch, T. Jansen, R. Pöttgen and T. Jüstel, Temperature dependent optical properties of red emitting Na_3GaF_6:Mn^{4+} as a color converter for warm white LEDs, *Z. Krist.*, 2018, **233**, 489–499.

29 M. G. Brik, S. J. Camardello and A. M. Srivastava, Influence of covalency on the Mn^{4+} $^2E_g \rightarrow {}^4A_{2g}$ emission energy in crystals, *ECS J. Solid State Sci. Technol.*, 2015, **4**, R39–R43.

30 M. G. Brik, S. J. Camardello, A. M. Srivastava, N. M. Avram and A. Suchocki, Spin-forbidden transitions in the spectra of transition metal ions and nephelauxetic effect, *ECS J. Solid State Sci. Technol.*, 2016, **5**, R3067–R3077.

31 A. M. Srivastava and M. G. Brik, The dependence of 10 Dq crystal field parameter for Mn^{4+} ($3d^3$ configuration) and the magnitude of $^7F_1$ level splitting for Eu^{3+} ($4f^6$ configuration) on pyrochlore compositions, *Opt. Mater.*, 2012, **35**, 196–200.

32 A. M. Srivastava and M. G. Brik, Crystal field studies of the Mn^{4+} energy levels in the perovskite, $LaAlO_3$, *Opt.*

Mater., 2013, **35**, 1544–1548.

33 T. Jansen, T. Jüstel, M. Kirm, S. Vielhauer, N. M. Khaidukov and V. N. Makhov, Composition dependent spectral shift of Mn^{4+} luminescence in silicate garnet hosts $CaY_2M_2Al_2SiO_{12}$ (M = Al, Ga, Sc), *J. Lumin.*, 2018, **198**, 314–319.

34 L. Wang, Z. Dai, R. Zhou, B. Qu and X. C. Zeng, Understanding the quenching nature of Mn^{4+} in wide band gap inorganic compounds: design principles for Mn^{4+} phosphors with higher efficiency, *Phys. Chem. Chem. Phys.*, 2018, **20**, 16992–16999.

35 T. Senden, R. J. A. van Dijk-Moes and A. Meijerink, Quenching of the red Mn^{4+} luminescence in Mn^{4+}-doped fluoride LED phosphors, *Light Sci. Appl.*, 2018, **7**, 8.